



# Engineering the electronic structure of platinum single-atom sites via tailored porous carbon nanofibers for large-scale hydrogen production

Ying Han<sup>a,1</sup>, Hengli Duan<sup>b,1</sup>, Wei Liu<sup>c,1</sup>, Chenhui Zhou<sup>a</sup>, Baoshun Wang<sup>a</sup>, Qinyuan Jiang<sup>a</sup>, Sihua Feng<sup>b</sup>, Wensheng Yan<sup>b</sup>, Ting Tan<sup>c,\*</sup>, Rufan Zhang<sup>a,\*</sup>

<sup>a</sup> Beijing Key Laboratory of Green Chemical Reaction Engineering and Technology, Department of Chemical Engineering, Tsinghua University, Beijing 100084, China

<sup>b</sup> National Synchrotron Radiation Laboratory, University of Science and Technology of China, Hefei 230029, China

<sup>c</sup> Laboratory of Theoretical and Computational Nanoscience, CAS Key Laboratory of Nanophotonic Materials and Devices, National Center for Nanoscience and Technology, Chinese Academy of Sciences, University of Chinese Academy of Sciences, Beijing 100190, China

## ARTICLE INFO

### Keywords:

Pt single-atom catalysts  
Electronic structure  
Carbon nanofibers  
Hydrogen evolution reaction  
Electrospinning

## ABSTRACT

Pt single-atom catalysts are promising for efficient hydrogen evolution reactions (HER) due to their ultra-high catalytic activity and atomic utilization. However, developing a scalable preparation method of binder-free Pt single-atom catalysts with optimal electronic structures for large-scale hydrogen production is still a serious challenge. In this work, we fabricated tailored nitrogen-doped porous carbon nanofibers as a support for engineering the electronic structure of Pt single-atom sites via initial micropore trapping and subsequent optimized nitrogen/carbon anchoring. The as-prepared Pt single-atom catalysts exhibited impressively enhanced HER activity and satisfactory stability, superior to the state-of-the-art single-atom catalysts. X-ray absorption structure analysis combined with theoretical simulation demonstrated the mechanisms for HER performance improvement. In particular, the free-standing Pt single-atom catalysts for a binder-free electrode showed a low overpotential of 64 mV even at 500 mA cm<sup>-2</sup>, indicating promising application for the large-scale hydrogen production.

## 1. Introduction

Nowadays, the problems of environmental pollution and energy shortage are becoming increasingly urgent. Among various types of new energy materials and technologies, hydrogen (H<sub>2</sub>) has attracted extensive attention for many years because of its merits of high calorific value, pollution-free combustion reactants, and abundant resources, etc [1]. The key to the wide application of hydrogen is how to produce hydrogen at low costs. Among various hydrogen production technologies, electrochemical hydrogen evolution reaction (HER) is a promising hydrogen production technology due to its low cost, environmental friendliness, and high hydrogen production purity [2,3]. At present, platinum-based catalyst is considered as the most efficient HER catalyst because of its excellent intrinsic reactivity [4,5]. However, the high cost and low earth reserve of platinum seriously limit their large-scale application. In recent years, non-platinum-based catalysts such as metal nitrides, sulfides, and phosphides have been widely investigated, but their activity and stability still need to be further improved [5–7]. The status of

platinum-based catalysts for HER still cannot be completely replaced. It is crucial to conduct rational structural design of platinum-based catalysts to achieve efficient atom utilization and improved electrochemical performance for the further development of HER catalysts [8].

Increasing the number of active sites and enhancing the intrinsic activity of each active site are two critical strategies for designing efficient HER catalysts [9]. In 2011, Zhang et al. proposed the concept of single-atom catalysis, in which metals were dispersed on the support in the form of isolated atoms [10]. In single-atom catalysts (SACs), the utilization ratio of metal atoms approaches 100 %, and the unique coordination structure of metal atoms achieves high catalytic activity [11–15]. To date, researchers have successfully prepared Pt single-atom catalysts on various supports such as carbon materials [16–20], transition metal compounds [21–25], and MXenes [26]. In particular, carbon rich materials can effectively accelerate water dissociation kinetics through tunable electronic structural effects [27–29], which provides promising support candidates for Pt atoms [30,31]. According to the reported carbon-based Pt single-atom catalysts, the coordination

\* Corresponding authors.

E-mail addresses: [tant@nanocr.cn](mailto:tant@nanocr.cn) (T. Tan), [zhangrufan@tsinghua.edu.cn](mailto:zhangrufan@tsinghua.edu.cn) (R. Zhang).

<sup>1</sup> These authors contributed equally to this work.

environment of Pt atoms has a critical impact on their catalytic activity and stability [8, 32–35]. It is of great significance to reveal the interaction between Pt atoms and carbon support, which could provide useful guidance for the further exploration of efficient single-atom catalysts [36–39]. On the basis of designing coordination structures, the electrode structure of catalysts has an important influence on the HER performance [39]. As far as we know, the previously reported Pt-SACs were mainly in the form of powders [40,41], and inert polymer binders (e.g., Nafion) were usually needed for fabricating electrodes, which thus decreased the exposure of active sites and increased electrical resistance [42,43]. In addition, the scalable preparation of single-atom catalysts for large-scale efficient hydrogen production still faces a serious challenge.

Herein, we fabricated a unique nitrogen-doped porous carbon nanofiber (pCNFs) as support for engineering well-defined Pt single-atom catalysts (Pt-SA/pCNFs). The pCNFs with three-dimensional interconnected macro-porous architectures achieved efficient adsorption of Pt precursors due to their good hydrophilicity and strong microporous capillary forces. The tailored nitrogen and carbon synergistically anchored Pt atoms through strong interactions and formed Pt-N<sub>2</sub>C<sub>2</sub> coordination configuration. The Pt-SA/pCNFs exhibited impressively enhanced HER activity and excellent stability, which was superior to the state-of-the-art SACs. Theoretical simulations revealed that the Pt-N<sub>2</sub>C<sub>2</sub> sites had a smaller negative binding energy and a nearly zero Gibbs adsorbed free energy of H, implying higher structural stability and hydrogen production reactivity. Moreover, the free-standing Pt-SA/pCNFs was used as a binder-free electrode, which achieved an ultra-high current density of 500 mA cm<sup>-2</sup> at a low overpotential of 64 mV, indicating promising application for the large-scale hydrogen production.

## 2. Experimental section

### 2.1. Catalyst synthesis

#### 2.1.1. Preparation of ZIF-8 nanoparticles

In a typical preparation procedure, 4.461 g of Zn(NO<sub>3</sub>)<sub>2</sub>·6 H<sub>2</sub>O was dissolved in 300 mL of methanol to form solution A, while 9.852 g of 2-methylimidazole (MeIM) was dissolved in 150 mL of methanol to form solution B. Solution A was quickly poured into solution B under stirring. The mixture solution was magnetically stirred at room temperature for 24 h. The white powder was collected by centrifugation, washed several times with methanol, and dried at 80 °C for 12 h.

#### 2.1.2. Preparation of nitrogen-doped porous carbon nanofiber (pCNFs) and nitrogen-doped carbon nanofiber (CNFs)

pCNFs were fabricated via electrospinning and subsequent carbonization processes. In a typical procedure, 1.0 g of as-prepared ZIF-8 nanoparticles was dispersed in 10 mL of N, N-dimethylformamide (DMF) by sonication for 1 h. Next, 1.0 g of polyacrylonitrile (PAN, Mw = 150,000) was dissolved in the above solution under constant stirring for 10 h. The electrospinning procedure was carried out in the following parameters: stainless needle (22<sup>#</sup>), feed rate of 1.0 mL h<sup>-1</sup>, applied voltage of 20 kV, and spinneret-to-collector distance of 15 cm. The collected nanofiber film was dried at 80 °C for 12 h, and preoxidized in air at 230 °C for 3 h with a heating rate of 1 °C min<sup>-1</sup>, and then calcined in Ar at 900 °C for 2 h at 5 °C min<sup>-1</sup>. When cooled naturally to room temperature, pCNFs film can be obtained.

The preparation process of CNFs film was similar to that of pCNFs, except that the addition of ZIF-8 nanoparticles.

#### 2.1.3. Preparation of Pt-SA@pCNFs and Pt-SA@CNFs

Pt-SA@pCNFs were synthesized via impregnation and subsequent pyrolysis processes. In a typical procedure, 50 mg of as-prepared pCNFs film was immersed in 50 mL PtCl<sub>4</sub> solution (0.2 mmol L<sup>-1</sup>) and let it stand for 24 h at room temperature. After washing several times with deionised water, the film was dried at 50 °C. Finally, the sample was calcined at 100 °C for 1 h and 500 °C for 1 h with a ramp rate of 2 °C

min<sup>-1</sup> under Ar. When cooled naturally to room temperature, Pt-SA@pCNFs can be obtained. When CNFs film was chosen as the support, a similar procedure was used to obtain Pt-SA@CNFs.

### 2.2. Materials characterization

The morphology and microstructures of samples were characterized by JSM 7401F scanning electron microscope (JEOL Ltd., Japan), JEM-2010 transmission electron microscope (JEOL Ltd., Japan), and double spherical aberration-corrected FEI Titan Cubed Themis G2300 transmission electron microscope. The phase composition was investigated by X-ray powder diffraction (Bruker D8 advance diffractometer with Cu-Kα radiation (λ = 1.54056 Å)) and Micro-Raman spectrometer (Horiba-Jobin-Yvon LabRAM HR800). The specific surface area was measured using a QUADRASORB SI physical adsorption instrument. The surface chemical state characterization was performed using an ESCALAB 250Xi (Thermal Fisher) X-ray photoelectron spectrometer. The Pt L<sub>3</sub>-edge X-ray absorption fine structure spectra were measured at the 1W1B beamline of Beijing Synchrotron Radiation Facility (BSRF, China). The N K-edge and C K-edge XANES spectra were obtained at beamlines MCD-A and MCD-B (Soochow Beamline for Energy Materials) National Synchrotron Radiation Laboratory (NSRL, China). Inductive coupled plasma mass spectrometry was conducted using Agilent ICP-OES 725 ES.

### 2.3. Electrochemical measurement

The HER performances were evaluated on the CHI 760E electrochemical workstation in a three-electrode system. A glassy carbon electrode (4 mm) was used as working electrode, where a graphite rod and saturated Ag/AgCl electrode were used as counter electrode and reference electrode, respectively. All potentials were calibrated to the reversible hydrogen electrode (RHE) scale by the following equation: E<sub>RHE</sub> = E<sub>Ag/AgCl</sub> + 0.0592 × pH + 0.197 V.

The catalyst inks were prepared by dispersing 5 mg of catalyst in 950 μL of ethanol and water mixed solution (volume ratio = 1:1) and 50 μL of 5 % Nafion solution, followed by ultrasonication for at least 40 min. Subsequently, 10.0 μL of Pt-SA@pCNFs catalysts slurry was drop-casted onto freshly polished working electrode. After drying in the air naturally, the mass loading of catalyst was approximately 0.40 mg cm<sup>-2</sup>. For comparison, the drop volumes for commercial 20 % Pt/C catalyst and Pt-SA@CNFs catalysts were chosen to be 5 and 15 μL, respectively. For manufacturing the binder-free electrodes, a Pt-SA/pCNFs film was sandwiched between two pieces of clean copper foam, followed by a laminating process.

Before the HER test, nitrogen was bubbled in the 0.5 M H<sub>2</sub>SO<sub>4</sub> solution for 30 min. Cyclic voltammetry (CV) at a scan rate of 100 mV s<sup>-1</sup> was carried out to activate the catalyst effectively. Linear sweep voltammetry (LSV) was conducted at a scan rate of 5 mV s<sup>-1</sup> and corrected by iR compensation. CV measurements in the non-Faradic potential region were performed for Pt SA@HCNFs. Chronopotentiometry tests were performed under a constant current density of 10 mA cm<sup>-2</sup>.

### 2.4. DFT calculations

The density functional theory (DFT) calculations with Perdew-Burke-Ernzerhof (PBE) functional were performed in the Vienna Ab-initio Simulation Package (VASP). The Projected Augmented Waves (PAW) pseudopotential was used to describe the core electrons, and an energy cutoff was set as 450 eV for the valence electrons. Grimme's DFT-D2 method was employed accounting for the long-range van der Waals interaction. A periodic 6 × 6 graphitic carbon slabs with a vacuum layer of 15 Å were built to simulate the Pt-N<sub>x</sub>C<sub>4-x</sub> structures. A 3 × 3 × 1 Monkhorst-Pack k-point mesh was used for all structures. Electronic energetics were converged to the criteria that the energy change is less than 10<sup>-5</sup> eV. Atomic relaxations were carried out until residual forces on each atom were smaller than 0.01 eV/Å.

The binding energy ( $E_{\text{bind}}$ ) of the  $\text{Pt-N}_x\text{C}_{4-x}$  systems was defined as:

$$E_{\text{bind}} = E_{\text{PtN}_x\text{C}_{4-x}} - E_{\text{Pt}} - E_{\text{N}_x\text{C}_{4-x}}$$

where the  $E_{\text{PtN}_x\text{C}_{4-x}}$ ,  $E_{\text{Pt}}$ , and the  $E_{\text{N}_x\text{C}_{4-x}}$  denote the energies of the  $\text{Pt-N}_x\text{C}_{4-x}$  systems, the single Pt atom, and the optimized defect substrate without Pt atom, respectively.

The hydrogen Gibbs adsorption free energy ( $\Delta G_{\text{H}^*}$ ) was calculated through  $\Delta G_{\text{H}^*} = \Delta E_{\text{H}^*} + \Delta E_{\text{ZPE}} - T\Delta S_{\text{H}}$ , where  $\Delta E_{\text{H}^*}$  was the hydrogen adsorption energy:

$$\Delta E_{\text{H}^*} = E_{(\text{Slabs}+\text{H}^*)} - E_{(\text{Slabs})} - \frac{1}{2}E_{\text{H}_2}$$

Besides,  $E_{(\text{Slabs}+\text{H}^*)}$  and  $E_{(\text{Slabs})}$  stand for the energies of  $\text{Pt-N}_x\text{C}_{4-x}$  structures with and without H adsorption, respectively. The zero-point energies ( $\Delta E_{\text{ZPE}}$ ) were obtained within the harmonic oscillator approximation.  $\Delta S_{\text{H}}$  was the change of the entropy of H from the gas phase state to the adsorption state. At room temperature ( $T = 298.15$  K),  $\Delta E_{\text{ZPE}} - T\Delta S_{\text{H}}$  was approximately 0.24 eV.

### 3. Results and discussions

#### 3.1. Pt single-atom catalysts synthesis and structures characterization

The fabrication of Pt-SA/pCNFs catalysts mainly includes

electrospinning, carbonization, impregnation, and pyrolysis processes (Fig. 1a). In the initial stage, a large number of as-prepared zeolite imidazole framework (ZIF-8) nanoparticles were uniformly dispersed in polyacrylonitrile (PAN) nanofibers via an electrospinning process. After the first carbonization process, PAN was transformed into an N-doped carbon skeleton, during which process the ZIF-8 nanoparticles could not only serve as sacrificial templates to form abundant microporous structures, but also significantly enhance the nitrogen doping in the carbon framework. Subsequently, sufficient platinum precursors were trapped by immersing the obtained porous carbon nanofibers into a platinum tetrachloride solution because of the high hydrophilicity and strong microporous capillary forces of the porous carbon nanofibers. During the subsequent pyrolysis process, nitrogen and carbon would coordinate with platinum atoms for strong anchoring, resulting in the atomic dispersion of platinum on the N-doped porous carbon nanofibers. For comparison, samples obtained under the parallel procedure without ZIF-8 were labelled as Pt-SA/CNFs.

Field-emission scanning electron microscopy (SEM) and transmission electron microscopy (TEM) were conducted to perform topographic analysis of the Pt-SA/pCNFs. As shown in Figs. 1b and 1c, the Pt-SA/pCNFs exhibited a diameter of approximately 400 nm, a rough surface, and an internal three-dimensionally interconnected macroporous architecture. In contrast, Pt-SA/CNFs had a smooth surface (Fig. S1a), and no obvious microporous structure was found (Fig. S1b).

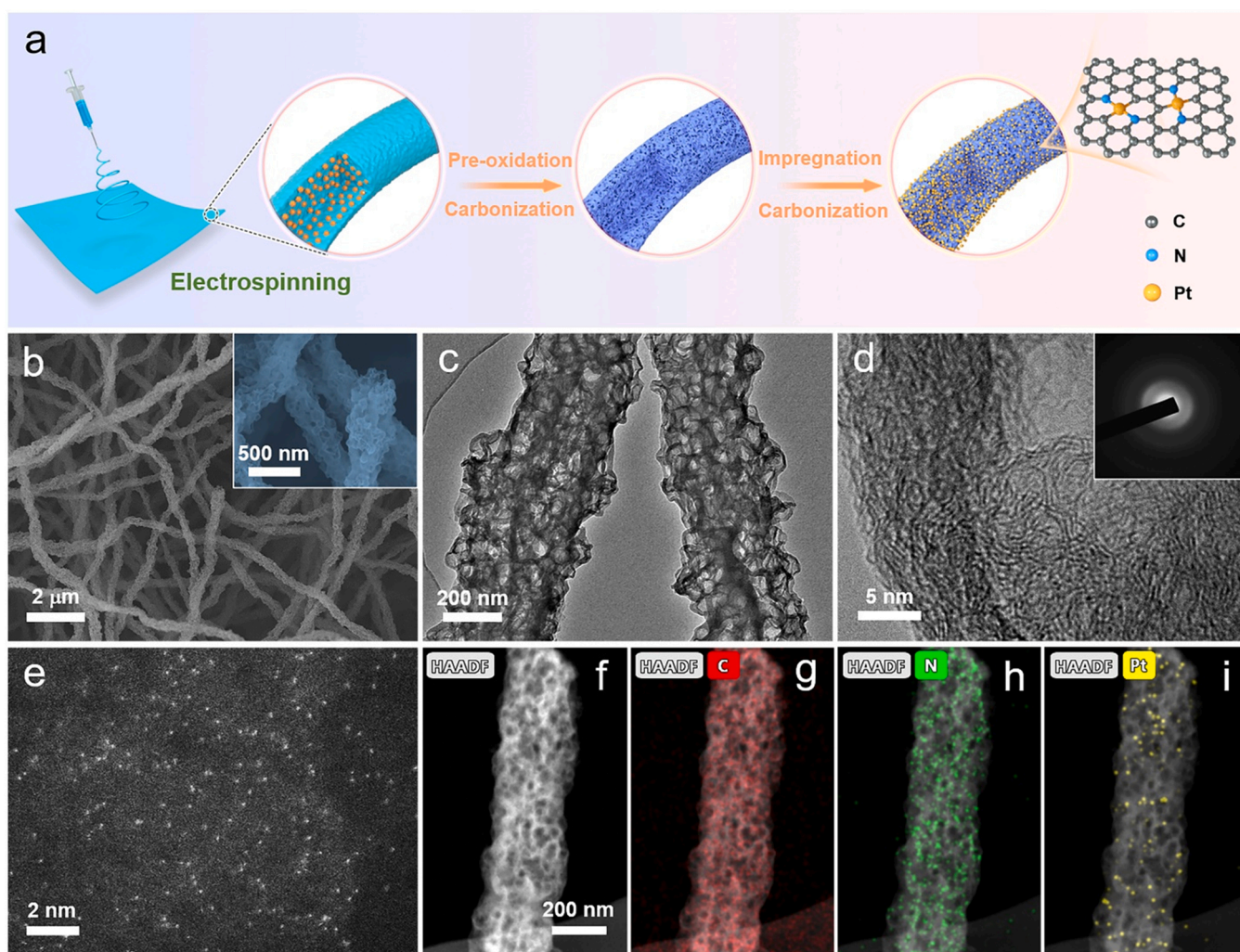


**Fig. 1.** Fabrication process and structural characterization of Pt-SA/pCNFs catalysts. (a) Schematic illustration for the fabrication of Pt-SA/pCNFs catalysts via electrospinning. (b) SEM image, (c) TEM images, (d) HR-TEM images and corresponding SAED pattern, and (e) AC HAADF-STEM image of the Pt-SA/pCNFs. (f-i) EDX elemental mapping of C, N, and Pt.



The Brunauer-Emmett-Teller (BET) surface area of Pt-SA/pCNFs was  $481.42 \text{ m}^2 \text{ g}^{-1}$ , which was much higher than that of Pt-SA/CNFs ( $31.98 \text{ m}^2 \text{ g}^{-1}$ ) (Fig. S5). The macro-porous architecture of Pt-SA/pCNFs was ascribed to the sacrificial templating role of ZIF-8 nanoparticles. In Fig. 1d, high-resolution TEM (HR-TEM) images combined with selected-area electron diffraction (SAED) pattern revealed the characteristics of typical amorphous materials. No lattice fringes or diffraction spots of metallic platinum were observed. Aberration-corrected high-angle annular dark-field scanning transmission electron microscopy (AC HAADF-STEM) further confirmed the dispersion of single platinum atoms (Fig. 1e). These individual bright dots revealed that platinum was well dispersed in the form of single atom. The energy dispersive spectroscopy (EDS) mapping images (Figs. 1f-1i) further demonstrated the uniform distribution of Pt, N, and C on the carbon matrix. Moreover, the amount of Pt in Pt SA/NHCs was determined to be 2.33 wt% according to the inductively coupled plasma optical emission spectrometer (ICP-OES) analysis. Whereas, the mass loading of Pt atoms was only 0.33 % wt% for Pt-SA/CNFs. The high mass loading of Pt atoms in Pt-SA/NHCs can be attributed to the micropore trapping effect of the abundant hierarchical porous structure in NHCs.

### 3.2. Chemical state and valence bonds for the catalysts

X-ray photoelectron spectroscopy (XPS) spectra was performed to elucidate the surface state of Pt-SA/pCNFs. As shown in Fig. 2a, the high-resolution N 1s spectrum could be deconvoluted into three sub-spectrums with peaks located at 398.5, 399.8, and 401.3 eV, corresponding to Pt-N bond/pyridinic N, pyrrolic N, and graphitic N, respectively. The content of pyridinic N was 52.7 %, which was higher than that of Pt-SA/CNFs (Table S2). Fig. 2b showed the Pt 4f XPS spectrum of Pt-SA/pCNFs, which can be deconvoluted into two kinds of Pt species. Two peaks at 72.4 and 75.8 eV could be attributed to the  $4f_{7/2}$  and  $4f_{5/2}$  orbitals of Pt (II) species, respectively, while those at 73.1 and 76.8 eV corresponded to the  $4f_{7/2}$  and  $4f_{5/2}$  orbitals of Pt (IV) species, respectively. In contrast, only two species of Pt (0) and Pt (II) were detected in 20 % Pt/C catalyst. The positive shift in the Pt 4f peaks of Pt-SA/pCNFs was closely related to the  $\text{Pt}^{\delta+}$  ( $0 < \delta < 4$ ) [37].

C and N K-edge X-ray absorption near-edge structure (XANES) measurements further probed the valence bonds of the Pt-SA/pCNFs. In the C K-edge XANES spectra of Pt-SA/pCNFs and Pt-SA/CNFs, a distinct peak located at 286 eV originated from graphitic C-C excitations, while the other peak at 293.0 eV was derived from graphitic C-C  $\sigma^*$  transitions (Fig. S7). It is worth noting that the difference at 289 eV indicates that Pt-SA/pCNFs have more obvious  $\pi^*$  resonance of the C-N bonds than Pt-

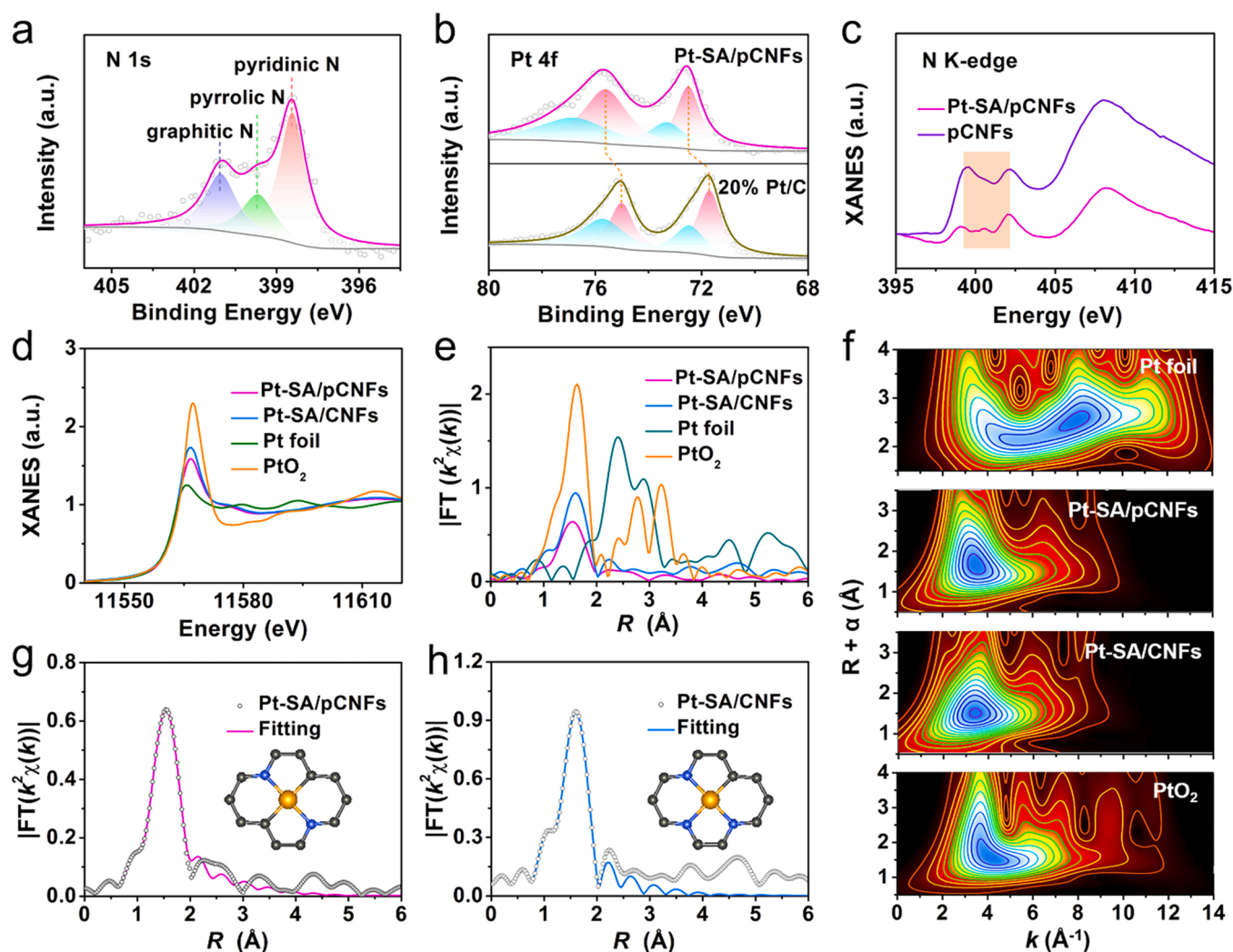


**Fig. 2.** Chemical state and valence bonds for the catalysts. (a) N 1s XPS spectra of Pt-SA/pCNFs. (b) Pt 4f XPS spectra of Pt-SA/pCNFs and 20 % Pt/C catalyst. (c) N K-edge XANES spectra for Pt-SA/pCNFs and pCNFs. (d) Pt L<sub>3</sub>-edge XANES spectra of the Pt-SA/pCNFs, Pt-SA/CNFs, PtO<sub>2</sub>, and Pt foil. (e) FT  $k^3$ -weighted Pt L<sub>3</sub>-edge EXAFS spectra, and (f) WT analysis of EXAFS spectra for Pt-SA/pCNFs and reference samples. (g) Pt L<sub>3</sub>-edge EXAFS fitting curves of the Pt-SA/pCNFs in R space. (h) Pt L<sub>3</sub>-edge EXAFS fitting curves of the Pt-SA/CNFs in R space.



SA/CNFs. In the N K-edge XANES spectra of PCNFs (Fig. 2c), four characteristic peaks of nitrogen were detected, among which the peaks located at 398.5 eV, 399.9 eV, 401.3 eV, and 407.2 eV could be attributed to the pyridinic N  $\pi^*$ , pyrrolic N, graphitic N  $\pi^*$ , and C-N  $\sigma^*$  transitions, respectively [42]. For Pt-SA/pCNFs, the pyrrolic peak remained constant, whereas the pyridinic peak was damped and split into two peaks, among which the new peak was derived from a portion of pyridinic N bonded to Pt atoms, which was consistent with previous reports [44].

Pt L<sub>3</sub>-edge XANES and extended X-ray absorption fine structure (EXAFS) analysis were performed to reveal the precise coordination environment and chemical state of Pt atoms in Pt-SA/pCNFs. According to the XANES analysis, the Pt L<sub>3</sub>-edge white-line (WL) intensity of Pt-SA/pCNFs and Pt-SA/CNFs laid between those of Pt foil and PtO<sub>2</sub> (Fig. 2d), indicating the positively charged state of Pt atoms in the as-prepared catalysts. The oxidation state estimated from the integrated area under the WL intensity of Pt L<sub>3</sub>-edge revealed an oxidation state of Pt (+2.11) in Pt-SA/pCNFs (Fig. S9). As depicted in Fig. 2e, the Fourier-transformed (FT)  $k^3$ -weighted Pt L<sub>3</sub>-edge EXAFS spectra of the Pt foil delivered a strong peak at 2.5 Å, which was originated from the metallic Pt-Pt bond. In contrast, the Pt-SA/pCNFs and Pt-SA/CNFs did not present such a

peak, further confirming the presence of Pt single atoms, which was consistent with the HAADF-STEM observation. Wavelet transform (WT) was performed to analyze the Pt L<sub>3</sub>-edge EXAFS oscillations (Fig. 2f). For Pt-SA/pCNFs and Pt-SA/CNFs, only one intensity maximum near 3.3 Å<sup>-1</sup> could be assigned to the C-Pt-N bonding, and no intensity maximum corresponding to Pt-Pt (~8 Å<sup>-1</sup>) was detected.

The coordination configuration of the Pt atom was further quantified by the least-squares EXAFS curve-fitting analysis. The fitting results from EXAFS Fourier-transformed (FT) features in Fig. 2g showed that the first shell of the central Pt atom possessed a coordination number of four with two N atoms and two C atoms. Based on Fig. 2g and Table S3, the Pt atom in the Pt-SA/pCNFs possesses a unique coordination structure of Pt-N<sub>2</sub>C<sub>2</sub> (inserted in Fig. 2g). Furthermore, by normalizing the Bader charge, the oxidation valence state of Pt in Pt-N<sub>2</sub>C<sub>2</sub> was estimated to be +2.23 (Fig. S10), which was close to that (+2.11) derived from XANES analysis [17]. In contrast, Pt L<sub>3</sub>-edge EXAFS fitting curves of the Pt-SA/CNFs revealed that the coordination configuration of Pt atom in Pt-SA/CNFs was Pt-N<sub>3</sub>C (inserted in Fig. 2h). The oxidation valence state of Pt in Pt-N<sub>3</sub>C was also consistent with the XANES results (Figs. S9 and S10).

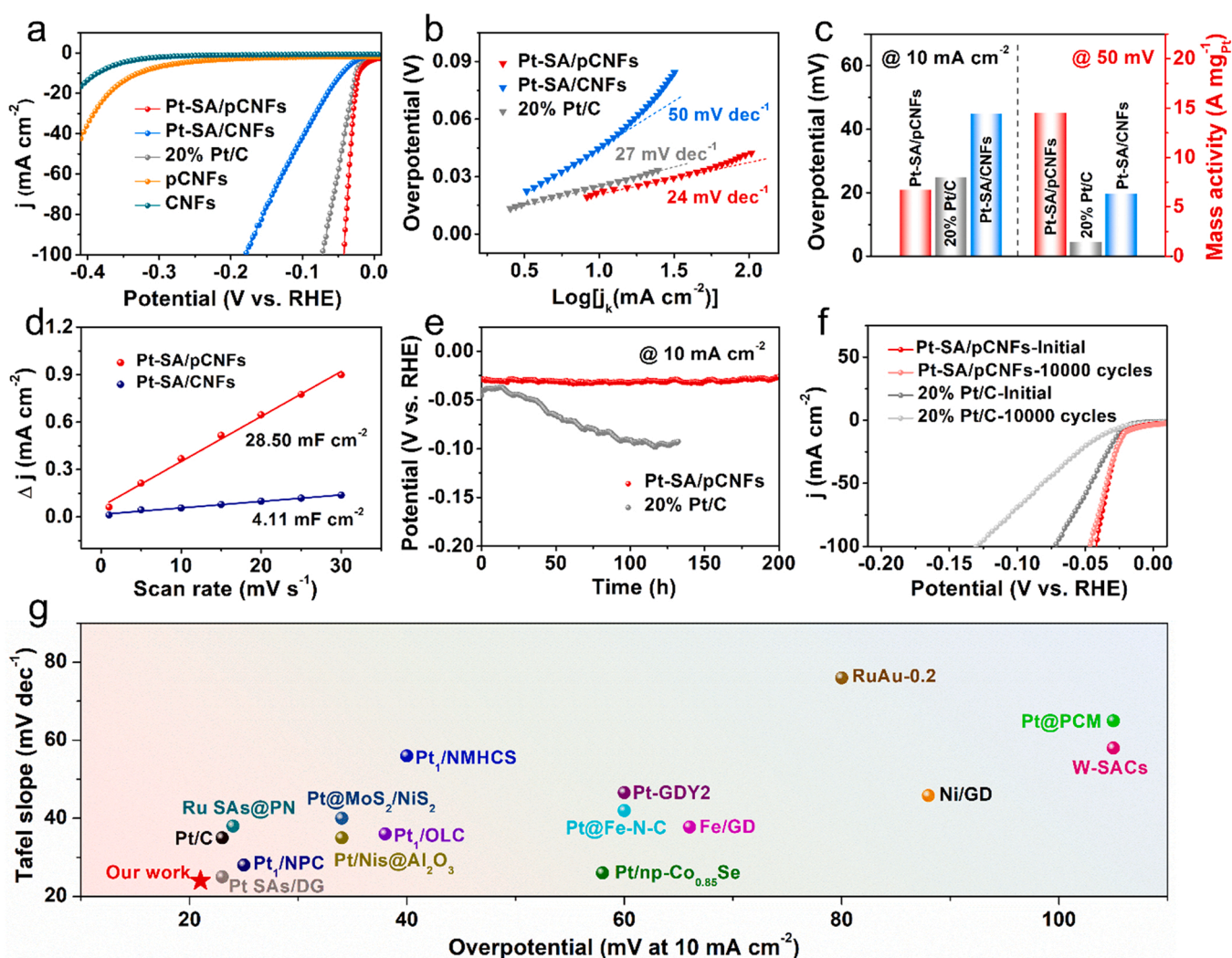


**Fig. 3.** Electrochemical performance of Pt-SA/pCNFs in a three-electrode system. (a) Polarization curves of the Pt-SA/pCNFs, Pt-SA/CNFs, 20 % Pt/C, pCNFs, and CNFs. (b) Tafel slopes of the Pt-SA/pCNFs, Pt-SA/CNFs and 20 % Pt/C. (c) Overpotential at 10 mA cm<sup>-2</sup> and mass activity at 50 mV of the Pt-SA/pCNFs, Pt-SA/CNFs and 20 % Pt/C, respectively. (d) C<sub>dl</sub> values of the Pt-SA/pCNFs and Pt-SA/CNFs. (e) Constant potential stability of Pt-SA/pCNFs and 20 % Pt/C. (f) Potential cycling stability of Pt-SA/pCNFs and 20 % Pt/C. (g) The comparison of Tafel slope and overpotential at 10 mA cm<sup>-2</sup> between Pt-SA/pCNFs and other state-of-the-art electrocatalysts.

### 3.3. HER electrocatalytic activities

The HER performance was evaluated in a N<sub>2</sub>-saturated 0.5 M H<sub>2</sub>SO<sub>4</sub> electrolyte. As shown in the linear sweep voltammetry (LSV) curves (Fig. 3a), the Pt-SA/pCNFs exhibited an excellent HER activity with a low overpotential of 21 mV at a current density of 10 mA cm<sup>-2</sup>. Even at 100 mA cm<sup>-2</sup>, the overpotential of Pt-SA/pCNFs was only 43 mV, which was lower than that of the Pt-SA/CNFs and 20 % Pt/C. The catalytic kinetics of catalysts were evaluated from the Tafel plots. The Pt-SA/pCNFs showed a Tafel slope of 24 mV dec<sup>-1</sup>, whereas the Pt-SA/CNFs and 20 % Pt/C exhibited Tafel slopes of 50 and 27 mV dec<sup>-1</sup>, respectively (Fig. 3b). The Tafel slope reflects the rate-determining step (RDS) of a catalytic process. We also evaluated the overpotential at 10 mA cm<sup>-2</sup> and mass activity at 50 mV of the Pt-SA/pCNFs, Pt-SA/CNFs, and 20 % Pt/C, respectively (Fig. 3c). The Pt-SA/pCNFs exhibited the lowest overpotential at 10 mA cm<sup>-2</sup> and the highest mass activity at 50 mV. Furthermore, for a quantitative comparison of these three catalysts, the turnover frequency (TOF) values were calculated. Pt-SA/pCNFs exhibited a notable TOF (14.8 s<sup>-1</sup>) at 50 mV, which was nearly 3 times higher than that of Pt-SA/CNFs (Fig. S11). The electrochemically active surface area (ECSA), which was generally proportional to the double-layer capacitance (C<sub>dl</sub>) of the electrocatalyst, was also investigated. The C<sub>dl</sub> was calculated from the cyclic voltammetry (CV) measurements (Fig. S12). The C<sub>dl</sub> of Pt-SA/pCNFs was 28.50 mF cm<sup>-2</sup>, which was larger than that of Pt-SA/CNFs (Fig. 3d). This observation provided direct evidence for the enlarged ECSA with the decoration of Pt atoms into the matrix. The enlarged ECSA provides more active sites for enhanced HER activity. The result of HER catalyzing stability test at 10 mA cm<sup>-2</sup> showed negligible overpotential change in 200 h (Fig. 3e), demonstrating an excellent long-time durability of the Pt-SA/pCNFs catalysts. We further performed an accelerated degradation tests (ADTs) to evaluate the durability of Pt-SA/pCNFs by operating continuous 10,000 CV cycles. As shown in Fig. 3 f, the Pt-SA/pCNFs exhibited

outstanding stability after 10,000 CV cycles, with a slight increment of only 8 mV at 100 mA cm<sup>-2</sup>. Compared with the previously reported state-of-the-art HER electrocatalysts, Pt-SA/pCNFs exhibited an obviously improved catalytic activity (Fig. 3 g, Table S6).

### 3.4. The mechanisms analysis for HER performance improvement

To obtain an in-depth insight into the principles of Pt sites with tailored coordination structures for HER process, a density functional theory (DFT)-based calculation was performed. Herein, we demonstrated the atomic structure of three well-defined Pt sites (i.e., Pt-N<sub>4</sub>, Pt-N<sub>3</sub>C, and Pt-N<sub>2</sub>C<sub>2</sub>) in Fig. 4a and Fig. S15. We evaluated the stability of the three coordination structures by binding energy calculations as follows:  $E_{\text{bind}} = E_{\text{PtNxC}_4} - E_{\text{Pt}} - E_{\text{NxC}_4-x}$ . Fig. 4a showed the relative Pt binding energy  $\Delta E_{\text{bind}}$  ( $\Delta E_{\text{bind}} = E_{\text{bind-PtNxC}_4-x} - E_{\text{bind-PtN}_4}$ ) with respect to PtN<sub>4</sub>. The more negative value of  $\Delta E_{\text{bind}}$  indicated a more stable architecture. As shown in Fig. 4a and Table S4, the most stable Pt-N<sub>2</sub>C<sub>2</sub> configuration structure exhibited the smallest  $\Delta E_{\text{bind}}$  of -1.74 eV, which revealed its advantage in structural stability. Coordination environment of Pt single atom significantly influenced the HER performance, which was mainly reflected in as indicated by the Gibbs free energy of H adsorption ( $\Delta G_{\text{H}^*}$ ). As shown in Fig. 4b, the Pt-N<sub>2</sub>C<sub>2</sub> structure had a nearly zero  $\Delta G_{\text{H}^*}$  ( $\Delta G_{\text{H}^*} = -0.17$  eV) compared to the Pt-N<sub>4</sub> ( $\Delta G_{\text{H}^*} = 1.44$  eV) and Pt-N<sub>3</sub>C ( $\Delta G_{\text{H}^*} = 0.68$  eV), indicating that its superior HER reactivity.

The electronic structure analysis such as differential charge density and density of states was further performed to explore the origin of excellent catalytic performance. As presented in Fig. 4c, the electronegativity differences of the C atoms and N atoms adjacent to the Pt atom caused significant electronic perturbations, which could alter the electron distribution state on the central Pt atom. When the N atoms adjacent to the Pt atom were replaced by C atoms, the electron accumulation effect on the C<sub>x</sub>N<sub>4-x</sub> side was gradually suppressed. Moreover, the Bader charge analysis revealed that the electron depletion on the

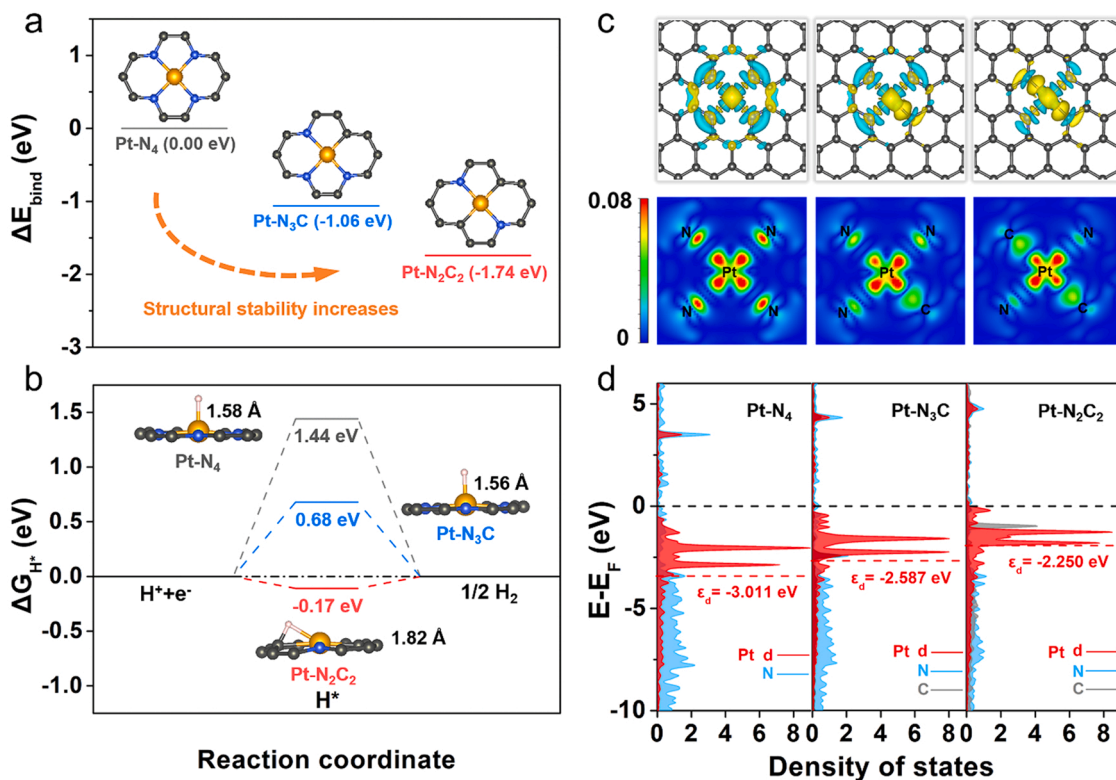


Fig. 4. DFT calculations for Pt sites with tailored coordination structures. (a) Binding energy of Pt-N<sub>3</sub>C and Pt-N<sub>2</sub>C<sub>2</sub> relative to PtN<sub>4</sub>. (b) Calculated  $\Delta G_{\text{H}^*}$  values of different Pt sites for HER in acidic conditions. (c) Nephogram of differential charge density. (d) PDOS for Pt-N<sub>4</sub>, Pt-N<sub>3</sub>C, and Pt-N<sub>2</sub>C<sub>2</sub> structures. The isosurface value was 0.004 e Å<sup>-3</sup>.



central Pt atom in the Pt-N<sub>2</sub>C<sub>2</sub> coordination structure (0.52 e<sup>-</sup>) was lower than that in Pt-N<sub>3</sub>C (0.59 e<sup>-</sup>) and Pt-N<sub>4</sub> (0.73 e<sup>-</sup>) structures (Table S5). That is to say, the Pt atom in Pt-N<sub>2</sub>C<sub>2</sub> structure with electron-rich state exhibited a stronger reduction ability for adsorbed H. Projected density of states (PDOS) was performed to rationalize the Pt-H bonding capacity trend of Pt-N<sub>x</sub>C<sub>4-x</sub>. By comparing with the PDOS of Pt-5d orbitals of Pt-N<sub>x</sub>C<sub>4-x</sub> (Fig. 4d), it was found that the d-band center of Pt-5d orbitals in Pt-N<sub>2</sub>C<sub>2</sub> (-2.250 eV) lies higher than that in Pt-N<sub>3</sub>C (-2.587 eV) and Pt-N<sub>4</sub> (-3.011 eV) with least occupation of anti-bonding states and strongest Pt-H interaction, which effectively mitigates the weak H-bonding of Pt-N<sub>3</sub>C and Pt-N<sub>4</sub>. Therefore, these results suggested that the coordination structure of Pt-N<sub>2</sub>C<sub>2</sub> processes much better HER activity than Pt-N<sub>3</sub>C and Pt-N<sub>4</sub>, leading to the different catalytic performance of Pt-SA/pCNFs and Pt-SA/CNFs.

### 3.5. Potential application for large-scale hydrogen production

The as-prepared Pt-SA/pCNFs can be directly used as binder-free catalysts for large-scale hydrogen production at ultra-low overpotentials. Herein, we used a copper foam as collector to demonstrate the potential of Pt-SA/pCNFs for efficient hydrogen production. As illustrated in Fig. 5a, the self-supporting Pt-SA/pCNFs combined with copper foam formed a binder-free work electrode via a laminating process. For contrast, the milled Pt-SA/pCNFs formed a binder-containing work electrode by dropping catalyst ink (containing Nafion) (Fig. 5b). At a high current density of 500 mA cm<sup>-2</sup>, the binder-free work electrode exhibited an ultra-low overpotential of 64 mV, while the overpotential of the binder-containing work electrode exceeded 110 mV (Fig. 5c). The inserted figure further revealed that the binder-free Pt-SA/pCNFs electrode could carry out stable hydrogen production at 500 mA cm<sup>-2</sup>. The enhanced catalytic activity of the binder-free electrodes was attributed to the direct contact of the active sites with the electrolyte. It was worth mentioning that Pt-SA/pCNFs showed impressive large-scale hydrogen production activity compared with the

previously reported state-of-the-art electrocatalysts (Fig. 5d, Table S7).

## 4. Conclusion

In summary, we proposed tailored nitrogen-doped porous carbon nanofibers as a support for engineering the coordination structure of Pt single-atom sites via initial micropore trapping and subsequent modulated nitrogen/carbon anchoring. X-ray absorption structure analysis revealed that the as-prepared Pt single-atom catalysts possessed the coordination structure of Pt-N<sub>2</sub>C<sub>2</sub>, and the theoretical simulation results further demonstrated the Pt-N<sub>2</sub>C<sub>2</sub> exhibited a higher structural stability and hydrogen production reactivity. The Pt-SA/pCNFs exhibited impressively enhanced HER activity and excellent stability, which was much better than the previously reported state-of-the-art single-atom catalysts. In particular, Pt-SA/pCNFs can be used as a binder-free electrode to achieve an ultra-high current density of 500 mA cm<sup>-2</sup> at a low overpotential of 64 mV, which was promising for the large-scale hydrogen production. This work precisely revealed the HER activity and stability of various Pt single-atom sites and provided a new route for the design and practical application of Pt-based catalysts.

### CRediT authorship contribution statement

Y.H. and R.Z. conceived the main idea of the project. R.Z. directed the whole project. Y.H. designed the experiments and wrote the paper. H.D., S.H., and W.Y. participated in the XANES characterization of the samples. W.L. and T.T. performed theoretical simulations and calculations. Y.H., W.L., C.Z., B.W., Q.J., and R.Z. participated the data analysis and discussion. The manuscript was written through contributions of all authors. All authors have given approval to the final version of the manuscript. Y.H., H.D., and W.L. contributed equally.

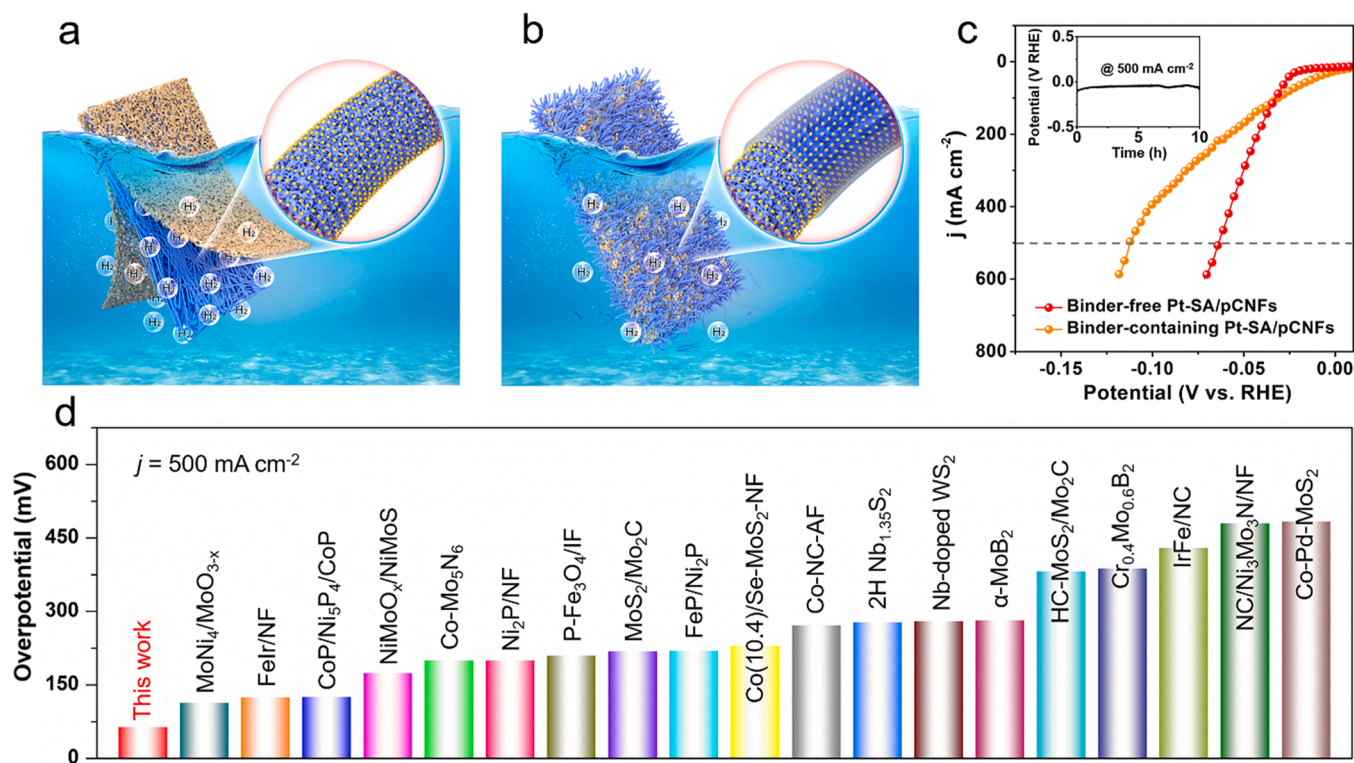


**Fig. 5.** Pt-SA/pCNFs for large-scale hydrogen production. (a) Schematic illustration for the self-supported Pt-SA/pCNFs as binder-free catalysts for HER. (b) Schematic illustration for the milled Pt-SA/pCNFs as binder-containing catalysts for HER. (c) Polarization curves of the Pt-SA/pCNFs for large-scale hydrogen production. (d) Comparison of the overpotential at 500 mA cm<sup>-2</sup> for the recently reported catalysts.



## Declaration of Competing Interest

The authors declare that they have no known competing financial interests or personal relationships that could have appeared to influence the work reported in this paper.

## Data availability

Data will be made available on request.

## Acknowledgement

This work was financially supported by the National Natural Science Foundation of China (Grant No. 22075163, 51872156, 22205010, 12105286), National Key Research Program (2020YFC2201100, 2020YFA0210700), and China Postdoctoral Science Foundation funded project (Grant 2020M670343). The authors thank the support of the Analytical and Testing Center of Tsinghua University. The authors also acknowledge the support of the 1W1B beamline of Beijing Synchrotron Radiation Facility (BSRF, China) and beamlines MCD-A and MCD-B (Soochow Beamline for Energy Materials) National Synchrotron Radiation Laboratory (NSRL, China).

## Appendix A. Supporting information

Supporting Information: SEM, TEM, HRTEM, and AC HAADF-STEM images of the Pt-SA/CNFs; SEM and TEM images of the precursor electrosynthesized film; additional XRD, Raman, XPS, BET, Pt L<sub>3</sub>-edge EXAFS fitting data; TOF value of the Pt-SA/pCNFs and Pt-SA/CNFs; Digital images of the self-supported catalysts. Supplementary data associated with this article can be found in the online version at [doi:10.1016/j.apcatb.2023.122898](https://doi.org/10.1016/j.apcatb.2023.122898).

## References

- [1] C.G. Morales-Guio, L.-A. Stern, X. Hu, Nanostructured hydrotreating catalysts for electrochemical hydrogen evolution, *Chem. Soc. Rev.* 43 (2014) 6555–6569.
- [2] J.N. Tiwari, S. Sultan, C.W. Myung, T. Yoon, N. Li, M. Ha, A.M. Harzandi, H. J. Park, D.Y. Kim, S.S. Chandrasekaran, Multicomponent electrocatalyst with ultralow Pt loading and high hydrogen evolution activity, *Nat. Energy* 3 (2018) 773–782.
- [3] F. Shen, Y. Wang, G. Qian, W. Chen, W. Jiang, L. Luo, S. Yin, Bimetallic iron-iridium alloy nanoparticles supported on nickel foam as highly efficient and stable catalyst for overall water splitting at large current density, *Appl. Catal. B* 278 (2020), 119327.
- [4] A.R. Zeradjanin, J.P. Grote, G. Polymeros, K.J. Mayrhofer, A critical review on hydrogen evolution electrocatalysis: re-exploring the volcano-relationship, *Electroanalysis* 28 (2016) 2256–2269.
- [5] J. Wang, F. Xu, H. Jin, Y. Chen, Y. Wang, Non-noble metal-based carbon composites in hydrogen evolution reaction: fundamentals to applications, *Adv. Mater.* 29 (2017) 1605838.
- [6] A. Ali, P.K. Shen, Nonprecious metal's graphene-supported electrocatalysts for hydrogen evolution reaction: fundamentals to applications, *Carbon Energy* 2 (2020) 99–121.
- [7] Y. Chen, J. Yu, J. Jia, F. Liu, Y. Zhang, G. Xiong, R. Zhang, R. Yang, D. Sun, H. Liu, W. Zhou, Metallic Ni<sub>3</sub>Mo<sub>2</sub>N porous microrods with abundant catalytic sites as efficient electrocatalyst for large current density and superstability of hydrogen evolution reaction and water splitting, *Appl. Catal. B* 272 (2020), 118956.
- [8] L. Zhang, K. Doyle-Davis, X. Sun, Pt-Based electrocatalysts with high atom utilization efficiency: from nanostructures to single atoms, *Energy Environ. Sci.* 12 (2019) 492–517.
- [9] Z.W. Seh, J. Kibsgaard, C.F. Dickens, I. Chorkendorff, J.K. Nørskov, T.F. Jaramillo, Combining theory and experiment in electrocatalysis: insights into materials design, *Science* 355 (2017) eaad4998.
- [10] B. Qiao, A. Wang, X. Yang, L.F. Allard, Z. Jiang, Y. Cui, J. Liu, J. Li, T. Zhang, Single-atom catalysis of CO oxidation using Pt<sub>1</sub>/FeO<sub>x</sub>, *Nat. Chem.* 3 (2011) 634–641.
- [11] Y. Gu, B. Xi, H. Zhang, Y. Ma, S. Xiong, Activation of Main-Group Antimony Atomic Sites for Oxygen Reduction Catalysis, *Angew. Chem. Int. Ed* 61 (2022), e202202200.
- [12] C. Zhu, S. Fu, Q. Shi, D. Du, Y. Lin, Single-atom electrocatalysts, *Angew. Chem. Int. Ed.* 56 (2017) 13944–13960.
- [13] Y. Chen, S. Ji, C. Chen, Q. Peng, D. Wang, Y. Li, Single-atom catalysts: synthetic strategies and electrochemical applications, *Joule* 2 (2018) 1242–1264.
- [14] D. Zhao, Z. Zhuang, X. Cao, C. Zhang, Q. Peng, C. Chen, Y. Li, Atomic site electrocatalysts for water splitting, oxygen reduction and selective oxidation, *Chem. Soc. Rev.* 49 (2020) 2215–2264.
- [15] Q. Shi, S. Hwang, H. Yang, F. Ismail, D. Su, D. Higgins, G. Wu, Supported and coordinated single metal site electrocatalysts, *Mater. Today* 37 (2020) 93–111.
- [16] H. Wei, K. Huang, D. Wang, R. Zhang, B. Ge, J. Ma, B. Wen, S. Zhang, Q. Li, M. Lei, Iced photochemical reduction to synthesize atomically dispersed metals by suppressing nanocrystal growth, *Nat. Commun.* 8 (2017) 1490.
- [17] Y. Qu, B. Chen, Z. Li, X. Duan, L. Wang, Y. Lin, T. Yuan, F. Zhou, Y. Hu, Z. Yang, Thermal emitting strategy to synthesize atomically dispersed Pt metal sites from bulk Pt metal, *J. Am. Chem. Soc.* 141 (2019) 4505–4509.
- [18] S. Ye, F. Luo, Q. Zhang, P. Zhang, T. Xu, Q. Wang, D. He, L. Guo, Y. Zhang, C. He, Highly stable single Pt atomic sites anchored on aniline-stacked graphene for hydrogen evolution reaction, *Energy Environ. Sci.* 12 (2019) 1000–1007.
- [19] H. Zhang, P. An, W. Zhou, B.Y. Guan, P. Zhang, J. Dong, X.W. Lou, Dynamic traction of lattice-confined platinum atoms into mesoporous carbon matrix for hydrogen evolution reaction, *Sci. Adv.* 4 (2018), eaao6657.
- [20] D. Liu, X. Li, S. Chen, H. Yan, C. Wang, C. Wu, Y.A. Haleem, S. Duan, J. Lu, B. Ge, Atomically dispersed platinum supported on curved carbon supports for efficient electrocatalytic hydrogen evolution, *Nat. Energy* 4 (2019) 512–518.
- [21] L. Zhang, L. Han, H. Liu, X. Liu, J. Luo, Potential-cycling synthesis of single platinum atoms for efficient hydrogen evolution in neutral media, *Angew. Chem. Int. Ed.* 56 (2017) 13694–13698.
- [22] Y. Guan, Y. Feng, J. Wan, X. Yang, L. Fang, X. Gu, R. Liu, Z. Huang, J. Li, J. Luo, Nanodiamond-like MoS<sub>2</sub>/NiS<sub>2</sub> with single platinum atoms doping as an efficient and stable hydrogen evolution reaction catalyst, *Small* 14 (2018), 1800697.
- [23] J. Li, Q. Guan, H. Wu, W. Liu, Y. Lin, Z. Sun, X. Ye, X. Zheng, H. Pan, J. Zhu, Highly active and stable metal single-atom catalysts achieved by strong electronic metal-support interactions, *J. Am. Chem. Soc.* 141 (2019) 14515–14519.
- [24] K. Jiang, B. Liu, M. Luo, S. Ning, M. Peng, Y. Zhao, Y.-R. Lu, T.-S. Chan, F.M. de Groot, Y. Tan, Single platinum atoms embedded in nanoporous cobalt selenide as electrocatalyst for accelerating hydrogen evolution reaction, *Nat. Commun.* 10 (2019) 1743.
- [25] Y. Shi, W.-M. Huang, J. Li, Y. Zhou, Z.-Q. Li, Y.-C. Yin, X.-H. Xia, Site-specific electrodeposition enables self-terminating growth of atomically dispersed metal catalysts, *Nat. Commun.* 11 (2020) 4558.
- [26] J. Zhang, Y. Zhao, X. Guo, C. Chen, C.-L. Dong, R.-S. Liu, C.-P. Han, Y. Li, Y. Gogotsi, G. Wang, Single platinum atoms immobilized on an MXene as an efficient catalyst for the hydrogen evolution reaction, *Nat. Catal.* 1 (2018) 985–992.
- [27] F. Cheng, X. Peng, L. Hu, B. Yang, Z. Li, C.-L. Dong, J.-L. Chen, L.-C. Hsu, L. Lei, Q. Zheng, M. Qiu, L. Dai, Y. Hou, Accelerated water activation and stabilized metal-organic framework via constructing triangular active-regions for amperometric current density hydrogen production, *Nat. Commun.* 13 (2022) 6486.
- [28] Q. Dai, L. Wang, K. Wang, X. Sang, Z. Li, B. Yang, J. Chen, L. Lei, L. Dai, Y. Hou, Accelerated water dissociation kinetics by electron-enriched cobalt sites for efficient alkaline hydrogen evolution, *Adv. Funct. Mater.* 32 (2022), 2109556.
- [29] F. Cheng, L. Wang, H. Wang, C. Lei, B. Yang, Z. Li, Q. Zhang, L. Lei, S. Wang, Y. Hou, Boosting alkaline hydrogen evolution and Zn-H<sub>2</sub>O cell induced by interfacial electron transfer, *Nano Energy* 71 (2020), 104621.
- [30] H. Fei, J. Dong, D. Chen, T. Hu, X. Duan, I. Shakir, Y. Huang, X. Duan, Single atom electrocatalysts supported on graphene or graphene-like carbons, *Chem. Soc. Rev.* 48 (2019) 5207–5241.
- [31] M.B. Gawande, P. Fornasiero, R. Zboril, Carbon-based single-atom catalysts for advanced applications, *ACS Catal.* 10 (2020) 2231–2259.
- [32] W.H. Lai, Z. Miao, Y.X. Wang, J.Z. Wang, S.L. Chou, Atomic-local environments of single-atom catalysts: synthesis, electronic structure, and activity, *Adv. Energy Mater.* 9 (2019) 1900722.
- [33] B. Lu, Q. Liu, S. Chen, Electrocatalysis of single-atom sites: impacts of atomic coordination, *ACS Catal.* 10 (2020) 7584–7618.
- [34] Y. Lei, Y. Wang, Y. Liu, C. Song, Q. Li, D. Wang, Y. Li, Designing atomic active centers for hydrogen evolution electrocatalysts, *Angew. Chem. Int. Ed.* 59 (2020) 20794–20812.
- [35] Y. Zhang, J. Yang, R. Ge, J. Zhang, J.M. Cairney, Y. Li, M. Zhu, S. Li, W. Li, The effect of coordination environment on the activity and selectivity of single-atom catalysts, *Coord. Chem. Rev.* 461 (2022), 214493.
- [36] X.P. Yin, H.J. Wang, S.F. Tang, X.L. Lu, M. Shu, R. Si, T.B. Lu, Engineering the coordination environment of single-atom platinum anchored on graphdiyne for optimizing electrocatalytic hydrogen evolution, *Angew. Chem. Int. Ed.* 57 (2018) 9382–9386.
- [37] P. Kuang, Y. Wang, B. Zhu, F. Xia, C.W. Tung, J. Wu, H.M. Chen, J. Yu, Pt single atoms supported on n-doped mesoporous hollow carbon spheres with enhanced electrocatalytic H<sub>2</sub>-evolution activity, *Adv. Mater.* 33 (2021), 2008599.
- [38] Q. Yang, H. Liu, P. Yuan, Y. Jia, L. Zhuang, H. Zhang, X. Yan, G. Liu, Y. Zhao, J. Liu, Single carbon vacancy traps atomic platinum for hydrogen evolution catalysis, *J. Am. Chem. Soc.* (2022) 2171–2178.
- [39] W. Yang, S. Chen, Recent progress in electrode fabrication for electrocatalytic hydrogen evolution reaction: a mini review, *Chem. Eng. J.* 393 (2020), 124726.
- [40] Z. Pu, I.S. Amiin, R. Cheng, P. Wang, C. Zhang, S. Mu, W. Zhao, F. Su, G. Zhang, S. Liao, Single-atom catalysts for electrochemical hydrogen evolution reaction: recent advances and future perspectives, *Nano Micro Lett.* 12 (2020) 21.
- [41] P. Aggarwal, D. Sarkar, K. Awasthi, P.W. Menezes, Functional role of single-atom catalysts in electrocatalytic hydrogen evolution: current developments and future challenges, *Coord. Chem. Rev.* 452 (2022), 214289.

- [42] Y. Han, H. Duan, C. Zhou, H. Meng, Q. Jiang, B. Wang, W. Yan, R. Zhang, Stabilizing cobalt single atoms via flexible carbon membranes as bifunctional electrocatalysts for binder-free zinc-air batteries, *Nano Lett.* 22 (2022) 2497–2505.
- [43] T.Y. Ma, S. Dai, S.Z. Qiao, Self-supported electrocatalysts for advanced energy conversion processes, *Mater. Today* 19 (2016) 265–273.
- [44] S. Fang, X. Zhu, X. Liu, J. Gu, W. Liu, D. Wang, W. Zhang, Y. Lin, J. Lu, S. Wei, Uncovering near-free platinum single-atom dynamics during electrochemical hydrogen evolution reaction, *Nat. Commun.* 11 (2020) 1029.